Carbon 204 (2023) 434–446

Contents lists available at ScienceDirect

Carbon

journal homepage: www.elsevier.com/locate/carbon

An eco-friendly solution for liquid phase exfoliation of graphite under optimised ultrasonication conditions

Justin A. Morton [a,*], Amanpreet Kaur [a], Mohammad Khavari [a,g], Anastasia V. Tyurnina [b], Abhinav Priyadarshi [a], Dmitry G. Eskin [b], Jiawei Mi [c], Kyriakos Porfyrakis [d], Paul Prentice [e], Iakovos Tzanakis [a,f]

[a] School of Engineering, Computing and Mathematics, Oxford Brookes University, College Cl, Wheatley, Oxford, OX33 1HX, UK
[b] Brunel Centre for Advanced Solidification Technology, Brunel University London, Kingston Lane, London, UB8 3PH, UK
[c] Department of Engineering, University of Hull, Cottingham Rd, Hull, HU6 7RX, UK
[d] Faculty of Engineering and Science, University of Greenwich, Central Avenue, Chatham Maritime, Kent, ME4 4TB, UK
[e] Cavitation Laboratory, School of Engineering, University of Glasgow, University Avenue, Glasgow, G128QQ, UK
[f] Department of Materials, University of Oxford, Parks Road, Oxford OX1 3PH, UK
[g] School of Computing and Engineering, College of Science and Engineering, University of Derby, Derby, DE22 3AW, UK

A B S T R A C T

Ultrasonic assisted liquid phase exfoliation (ULPE) is a promising method for the large scale production of 2D materials. Currently, toxic solvents such as N-Methyl-2-pyrrolidone (NMP) are commonly used for the production of graphene. In this paper four solvents; three green solvents (water, ethanol and water/ethanol) plus NMP for comparison, were sonicated and examined in terms of their bubble dynamics and acoustic emissions. Advanced fundamental analysis was conducted using high-speed imaging synchronised with acoustic pressure measurements complemented by shadowgraphic photography of the emitted shockwaves, in order to determine a suitable eco-friendly solvent medium from a cavitation bubbles dynamics perspective. Thereafter, ULPE of graphite in the optimum solvent took place for 2 h under controlled ultrasonication parameters. The produced graphene samples were characterised by employing a series of techniques consisting of Ultraviolet–visible (UV–Vis) and Raman spectroscopy as well as transmission electron microscopy (TEM). A mixture of deionised water and ethanol was shown to produce a yield twice that of pure water, comprising of high quality few layer graphene (3–5 Ls) with an average area of ~1.15 $(\mu m)^2$ and stability of ~78% for the duration of six months. This combination is a promising eco-friendly substitute for future commercial manufacturing of graphene.

1. Introduction

Graphene was first isolated in 2004 by Novoselov et al. [1], which brought about an exciting new research field for the development and applications of two dimensional (2D) materials [2–7]. One effective method for producing 2D materials is liquid phase exfoliation (LPE), which has the capability for producing high quality 2D materials with large surface areas, appropriate for a wide range of applications [8]. This method was first tested by Coleman et al. in 2008 [9], and since then has gained success with additional complementing techniques such as high-shear mixing [10] or ultrasonication (ULPE) [11,12]. In most cases these complementary techniques are used for dispersion of chemically exfoliated graphene, although ULPE was demonstrated to be a powerful means for exfoliation by itself [13].

ULPE utilises energetic cavitation bubbles to facilitate material exfoliation. Powerful shear forces are provided via transient cavitation (generating shock waves (SW) and liquid-jets from bubble implosions) and stable cavitation (generating rapid oscillating forces). Our group recently demonstrated using *in situ*, high-speed imaging that different sono-exfoliation mechanisms occur during sonication [14]. SWs with a pressure magnitude up to 5 MPa and liquid-jets in the range of 80 ms^{-1} were revealed to initiate and propagate layer delamination. Additionally, stable cavitation bubbles were shown to vigorously oscillate between the split layers, expediting exfoliation in a fatigue manner. Other key findings showed that bulk layered graphite flakes within the cavitation zone (i.e. under a sonotrode tip) were subject to proliferation of layer tearing.

Recent development in the research of ULPE has led to high quality few-layer graphene (FLG) produced in relatively short periods of time (2 h) while using water as an environmentally friendly liquid medium [11,13]. Despite these advances, graphene yield and nano material stabilisation (as a consequence of water's surface tension promoting re-agglomeration) still impose limitations for broad exploitation and upscaling. Currently, N-Methyl-2-pyrrolidone (NMP) is considered the

* Corresponding author.
E-mail address: 18096707@Brookes.ac.uk (J.A. Morton).

https://doi.org/10.1016/j.carbon.2022.12.070
Received 31 October 2022; Received in revised form 20 December 2022; Accepted 26 December 2022
Available online 29 December 2022

optimum exfoliating agent for generating 2D materials via LPE [15,16] due to its chemical properties facilitating the dismantling of the Van der Waals bonding holding the stacked layers together. However, in addition to its toxic nature and difficulty of removal of NMP from the final exfoliated product, the energy consumption due to long sonication periods also poses an issue. Previous research has been able to produce increasing yields of graphene, but at the cost of numerous hours of sonication, which also decreases the size of the graphene sheets (smaller than 1 μm) [16,17].

One solution to overcome the drawbacks that NMP presents is to use eco-friendly solvents in combination with water that could exhibit appropriate cavitation behaviour while promoting high quality exfoliation and stability optimisation. Therefore, this study focused on investigating the effect of solvent selection and comparing eco-friendly solvents with NMP for ULPE. Deionised water (DIW), ethanol (EtOH), NMP and DIW:EtOH in a 50:50 (v/v) mixture were observed using high-speed imaging *in situ* for bubble dynamics and their respective cavitation zones generated under sonication with an ultrasonic horn. The rationale behind this specific choice of 50:50 DIW:EtOH ratio is due to its surface tension (23.91 mN/m) being close to the surface energy of graphite (23.93 mN/m), that promotes wettability and dispersibility as recently shown in Ref. [18] and hence provides more appropriate physical properties beneficial for high exfoliation efficiency of graphene than water or even NMP.

High-speed imaging observations were synchronised with real-time parallel acoustic pressure measurements using a calibrated fibre-optic hydrophone (FOH). Additionally, shadowgraphic ultra-high-speed imaging was taken to analyse SW generation in the solvents under investigation, as SWs have previously been identified as the primary exfoliating mechanism upon ULPE [14]. The resulting data enabled us to define sonication parameters for a promising eco-friendly solvent to produce high-quality graphene. In light of the obtained acoustic pressure measurements and high-speed images, ULPE of graphene in DIW (as a reference liquid used in many previous studies [13,16–19]) and DIW:EtOH (found to be the most promising candidate) was performed, followed by its in-depth spectroscopic and microscopic characterization to assess the quality of the final product. The experiments were conducted at 40 °C as this temperature was found to enhance ULPE results [20,21].

This study presents the first in-depth analysis comparing fundamental physical properties and *in situ* observations of bubble dynamics for a range of solvents used for ULPE, including NMP (currently the most commonly used, and best performing solvent for exfoliation of graphene). This research consists of two main sections. The first section comprised data acquisition and *in situ* high-speed imaging for the investigated solvents. The second section demonstrated ULPE processing of graphene in the identified solvents, i.e. DIW and DIW:EtOH, and their characterizations together with a comprehensive comparison of dispersed graphene in terms of its degree of exfoliation, quality and stability in both solvents.

2. Method

2.1. Synchronised high-speed imaging & data acquisition experimental setup

The solvents chosen to analyse for this study were DIW (Hexeal chemicals), EtOH (99.9%, Merck Life Sciences), NMP (Sigma-Aldrich), and a 1:1 ratio mix of DIW and EtOH. The mixture was investigated to establish an environmentally friendly replacement for NMP, a commonly used solvent for exfoliation of graphite. As such, the physical properties of DIW:EtOH were more alike to NMP (Table S1) i.e. a closer surface tension and viscosity, hypothesised to prevent re-agglomeration of exfoliated nano-sheets and reduce structural damage. A rectangular glass chamber (75 × 100 cm) was filled with 150 ml of the liquid medium under investigation.

A Hielscher UP200S with a 3-mm diameter titanium sonotrode and an operational frequency of 24 kHz was used for observation of generated bubble clouds and the cavitation zone. The peak-to-peak amplitude was set to 126 μm corresponding to an operating power of 60 W (60%), respectively. A smaller diameter sonotrode was used than that of the larger 22-mm (Section 2.3) as the entire sonotrode tip/cavitation zone cannot be observed at suitable quality to resolve *in situ,* in-depth bubble dynamics using high-speed imaging. In addition, the 3-mm sonotrode prevents blocking of the camera field of view from the populated bubbly structures ensuring more clear and accurate data for analysis. As the fundamental frequency is the same for both transducers, qualitative information on the bubble dynamics was reliable.

The solvent temperature was set to 40 ± 2 °C without the need for temperature control as only short ultrasonic pulses (~ 250 ms) were generated from the sonotrode. This temperature was selected as our group has previously found it to enhance ULPE results [20], and would aid in the specific solvent selection used to carry out long-term sonication in Section 2.2.

A calibrated FOH (Precision Acoustics Ltd) was used to measure acoustic pressures emitted from the cavitating bubbles and bubbly clouds. The calibration of the hydrophone was between 1 and 30 MHz, hence, within a frequency range ideal for detecting broadband SWs [22], which have previously been demonstrated to be the driving exfoliation mechanism [14].

The FOH sensor was positioned and fixed 3 mm below the sonotrode tip (to detect high energy cavitation activity ideal for exfoliating graphite). A Peripheral Component Interconnect (PCI) card was installed into the PC, with the high-speed camera and FOH connected to enable synchronisation of the imaging and pressure measurements (Fig. S1).

Cavitation intensity was captured using a digital oscilloscope (Picoscope 3000 series) connected to the calibrated FOH device, where 60 waveforms of cavitating emission signals were recorded and averaged. A bandpass filter was applied to disregard everything outside the calibration range and below 1 MHz. The corresponding readings were then converted to acoustic pressures using fast Fourier transform over a 2-ms time period with sampling rate of 500 × 10^6 samples/s. Intrinsic background noise was removed, by means of subtraction from the initial voltage signal. Both the Root means square pressure (P_{RMS}) and maximum pressure (P_{max}) were obtained and used to analyse the acoustic emissions. A step by step procedure on the calibration, signal processing and pressure conversion can be found elsewhere [22,23].

A Photron- SA-Z 2100K camera was used to record high-speed images in conjunction with the measured pressures, using a frame rate of 50,000 fps over 512 × 712 pixels with a shutter time of 16.25 μs A powerful front light beam LED flash lamp (GS Vitec) was used to provide illumination.

In order to measure acoustic pressures emitted from the sonotrode ideal for ULPE (Section 2.3), a Hielscher UP400St with a 22-mm diameter titanium sonotrode and an operational frequency of 24 kHz was used. The peak-to-peak amplitude was set to 9.2, 23 and 46 μm, corresponding to an operating power of 40, 200 and 400 W (20, 50 and 100%), respectively (acoustic intensity calculations for these powers can be found in Table S3). In this instance the FOH was positioned 22 mm below the sonotrode tip, with both P_{RMS} and P_{Max} calculated. Temperature conditions were set to 40 ± 2 C° for the solvents under investigation.

2.2. Shadowgraphic high-speed imaging experimental setup

The same solvents and chamber dimensions specified in Section 2.1 were used for shadowgraphic imaging.

To observe cavitation and SW generation for the solvents we opted for using the Hielscher UP200S (described in Section 2.1), this time with a 7-mm diameter titanium sonotrode attachment. This allowed for the best combination of observing cavitation activity in conjunction with the widest field of view available for imaging. High-speed

shadowgraphic videos were taken using a Shimadzu (HPV X2) camera capturing at 1 million frames per second (Fig. S2). For each recorded image sequence the camera generated 256 frames, producing shadowgraphic images with a resolution of 400 × 250 pixels. Instead of visible light illumination, collimated laser pulses enabled observation of propagating SWs from transient cavitation collapses. Synchronised 10 ns laser pulses through a collimating lens provided the illumination (CAVILUX Smart UHS system) and effective temporal resolution to observe the generated SWs.

2.3. Ultrasonic exfoliation of graphite & characterisation

Materials and solvents used in this study are listed below.

- Graphite powder (GP) (Alfa Aesar 300 mesh, maximum 56 μm) was used as received without any further modification.
- Ultra-Pure De-ionized water (DIW) (Hexeal Chemicals, UK).
- Ethanol (EtOH) (99.9%) (Merck Life Sciences, UK).
- Silicon wafers (Diameter 3", Orientation <100> from Pi-Kem, UK).
- Holey carbon coated copper grid (300 mesh, purchased from Agar Scientific, UK).
- Acetone (99.9%, Merck Life Sciences, UK), Isopropanol (99.9%, Merck Life Sciences, UK) for cleaning silicon wafers.
- Polytetrafluoroethylene (PTFE) membranes (Millipore, 0.2 μm pore size, 47 mm in diameter).

Herein, we have addressed a strategic methodology with illustrations and discussions of the protocols developed in our lab to optimize ULPE parameters for graphene exfoliation and resultant size selection followed by basic spectroscopic analysis and characterization of the optimized samples with state of art microscopic techniques.

To start with, 150 ml of DIW was filled in a double walled borosilicate glass beaker (Cole Parmer, 250 ml, 50 mm-diameter). The beaker was integrated to a recirculating cooler (Cole Parmer Stuart SRC5) through hose pipes allowing for temperature control. We performed the series of ULPE experiments in DIW and DIW:EtOH with different input powers of 33% (peak to peak amplitude ~ 15 μm), 50% (23 μm), 60% (27 μm), 80% (37 μm) and 100% (46 μm) at temperatures of 10 °C, 20 °C, 40 °C and 60 °C to optimize the processing parameters prior to executing the final experiment. The results are provided in Appendix A. Based on the outcomes of the results, we found that using an input power of 50% at 40 °C was the best suitable combination parameter among all; in part, based on our group's previous research [13,24]. For DIW:EtOH, 75 ml of DIW was homogeneously mixed with 75 ml of EtOH to make 50:50 v/v mixture. First, ultra-sonication was performed in DIW with a Heilscher UP400St (as described in Section 2.1) at 50% input power for 5–10 min with the cooler on, to achieve the constant solution temperature of 40 ± 0.1 °C (The additional details on power settings can be seen in Section 2.1 (Appendix A) of the Supplementary material). The probe tip was kept 10 mm below the liquid surface throughout the duration of the experiments. After attaining a constant solvent temperature of 40 ± 0.1 °C (verified with RS 52 Digital Thermometer), 60 mg of GP was added to the DIW and stirred with a glass stirrer until well mixed, followed by its ultra-sonication for an uninterrupted 2 h duration.

This experiment was further executed with the solvent DIW:EtOH mixture under the same experimental parameters (the additional details on power settings can be seen in Section 2.2 (Appendix A) of the Supplementary material). After sonication, dark graphene poly-dispersions of approx. 10 mℓ were pipetted from the upper part of the solution and near the tip of the sonotrode as one of our recent studies demonstrated proliferation of exfoliation within this region due to multiple, close range SW interactions with graphite particles [14]. Dispersions were then centrifuged at 1500 *g* RCF for 30 min using SciSpin One Benchtop centrifuge to sediment un-exfoliated graphite particles/thick flakes to obtain supernatants. The purpose for choosing 1500 *g* is that we have optimized this RCF value beforehand based on UV–Vis absorption results for analogous conditions and results are presented in Appendix B. After centrifugation, the top two-thirds of the supernatants were decanted via careful pipetting and retained as a final product for further characterizations, and labelled as DIW and DIW:EtOH samples.

Firstly, UV–Vis absorption spectra of the obtained supernatants were recorded in the wavelength range of 200–800 nm with Cary-60 spectrophotometer (Agilent Technologies) using quartz cuvettes (volume 3.5 ml, Agilent Technologies) with an optical path length of 10 mm. Dual-beam mode and baseline correction were used throughout the measurements to scan the samples. The spectra were recorded immediately after collecting supernatants to circumvent the agglomeration of flakes and scans were repeated a minimium of five times to obtain consistency in results. After getting reasonable findings from preliminary UV–Vis measurements, the examined supernatants were drop-casted onto a cleaned silicon substrate and dried in a vacuum oven prior to Raman investigations. Furthermore, micro-Raman analyses of the drop casted samples were performed with InVia spectrometer (Renishaw) at an excitation wavelength of 514 nm laser (2.33 eV). The laser power was kept below 1 mW in order to prevent sample damage and peak shift induced by the laser. Data collection was performed with 50 × magnification and acquisition time was adjusted accordingly to have a coherent signal/noise ratio. To obtain reliable results, Raman spectra of at least 20–30 random flakes were recorded for each sample in the range from 1200 to 3100 cm^{-1}. Simultaneouly, 2–3 drops were put onto holey carbon coated copper grid placed on a filter paper to wick away excess solvent and dried completely for TEM investigations. TEM analyses (both low magnification and high resolution) were performed to interrogate the individual flakes using a JEOL 2100F Field Emission Gun operating at 200 kV. Additionally, image processing was performed with *ImageJ* software to evaluate the quality and dimensional analyses of registered flakes to generate meaningful statistical data.

3. Results & discussion

3.1. Characterisation of cavitation phenomena in different solvents

3.1.1. High-speed imaging synchronised with acoustic measurements

For clarity, the nomenclature used to describe the cavitation activity should first be defined. For this study, the "primary" cavitation cloud refers to the large bubble cluster formed directly under the sonotrode tip. The "secondary" cavitation cloud refers to bubbles that separate from the primary cavitation cloud. These consist of satellite bubbles and bubble clusters. The "cavitation zone" refers to the overall spatial distribution of the cavitation bubbles.

The use of the FOH synchronised with high-speed imaging allowed for precision acoustic pressure measurements mapped to cavitation activity. Fig. 1 shows this synchronisation technique for the various solvents under investigation, whereby the cavitation intensity has been converted into acoustic pressure. We can see from observing the ultrasonication in DIW (Video 1 in Supplementary materials) that once the sonotrode was activated the first batch of acoustic emissions were detected from the FOH. During the first 2 ms after the activation, low cavitation intensity (represented by only a few spikes in the time domain signal) was measured, with no visible cavitation bubbles (Fig. 1(a)). However, after ~ 2.5 ms bubble nucleation occurred and coincided with the rise in cavitation intensity (represented by prominent spikes in the time domain signal) on the graph (Fig. 1(a)). During the next ~ 5 ms the camera footage (Video 1) showed an increase in size of the primary cavitation cloud, which again occurred in accordance with the increase in the measured cavitation intensity (as indicated by the red arrow). We have previously reported this phenomenon, noting that upon sonotrode activation, a higher intensity is recorded until a stabilised period is reached where the cavitation under the sonotrode tip remains stable, after which little variation in size occurs [14]. This rise in acoustic pressure can be seen for all plots in Fig. 1, where thereafter, a stable period was observed with generally lower acoustic pressures.

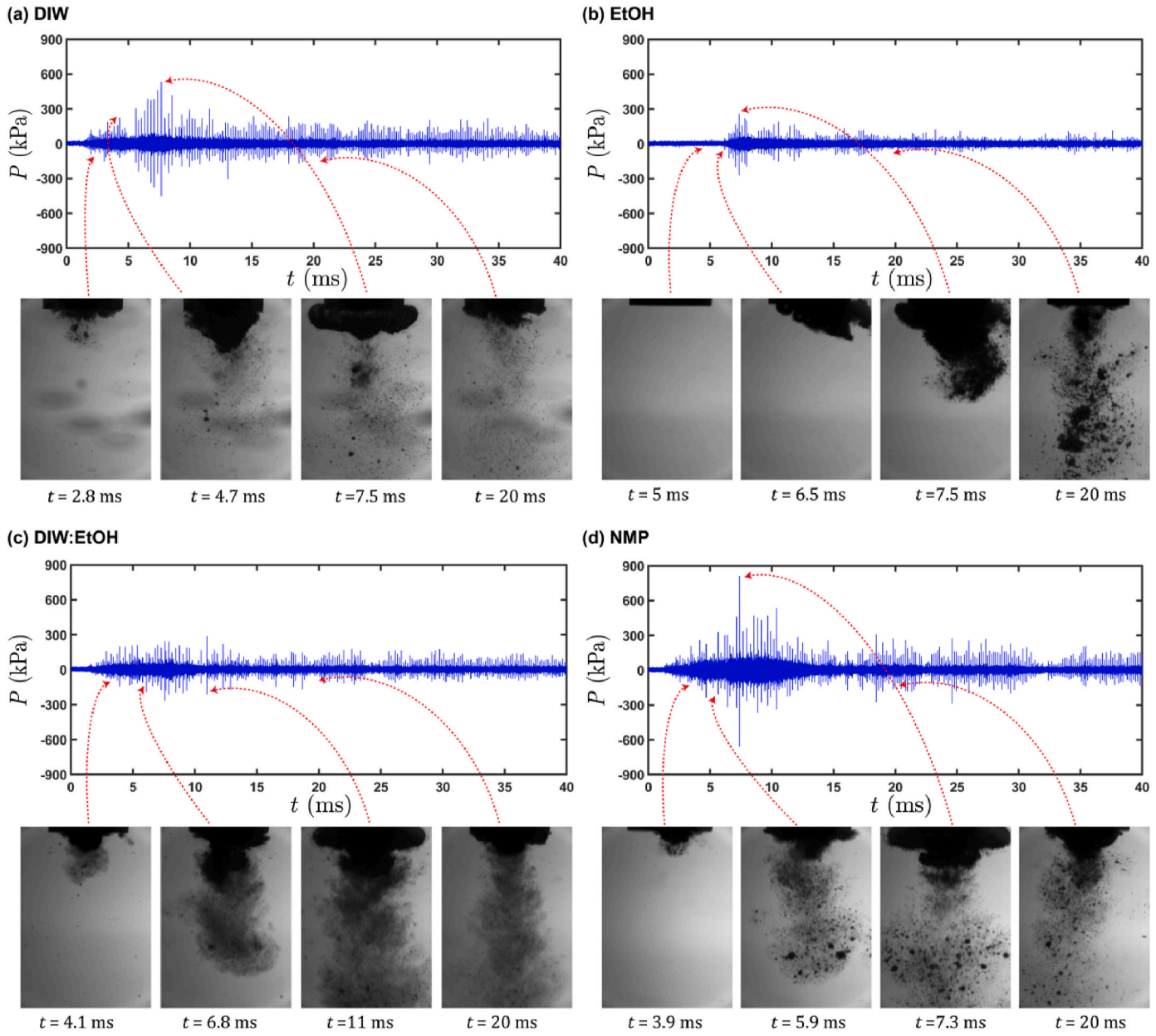

Fig. 1. Synchronised high-speed images (insets) with acoustic pressure plots from 0 to 40 ms for each solvent; **(a)** DIW, **(b)** EtOH, **(c)** DIW:EtOH & **(d)** NMP. The insets display four representative moments (indicated via the red arrows) of the developing bubble dynamics for each solvent; (1) initial activation of the sonotrode, (2) cavitation cloud development, (3) maximum cavitation cloud before collapse (thereafter, a large corresponding pressure spike is induced), (4) stabilised cavitation period. Imaging was taken at 50 kfps, with intensity measured via a FOH and converted to acoustic pressure. The transducer input power was set to 60% with the solution temperature at 40 °C. (A colour version of this figure can be viewed online.)

Interestingly, the EtOH solution took longer to generate observable cavitation bubbles (~ 6 ms, Fig. 1(b)), in addition to giving rise to the smallest pressure peaks than the other solvents under investigation. For DIW:EtOH, we observed more pressure peaks than EtOH, with larger intensities (Fig. 1(c)). NMP produced a pressure-time plot alike to DIW, with higher intensity peaks than EtOH and DIW:EtOH and also gave rise to the largest measured peak for all the solvents (Fig. 1(d), ~ 7.5 ms).

Supplementary video related to this article can be found at https://doi.org/10.1016/j.carbon.2022.12.070.

The recorded collapse of a bubble cloud under the sonotrode tip can be seen to produce a pressure spike on the graph. For instance, the highest measured acoustic pressure of EtOH (Fig. 1(b), next to the red arrow) at ~ 7.5 ms (generating ~ 300 kPa) coincided with the cavitation zone just after collapse (Video 2 in Supplemental materials). Images in Fig. 1 display four representative moments of developing bubble dynamics (specified in the caption). At ~ 7.5 ms for EtOH the image captures the large primary cloud formed under the sonotrode tip just before this collapse. After the cavitation cloud collapsed, multiple SWs were generated and detected by the FOH (indicated by the large pressure spikes, Fig. 1(b)). Often, a larger bubble cloud collapse will trigger transient bubble collapses sporadically from the secondary clouds and, hence, a higher measured intensity is registered via the FOH. However, this is not always the case due to acoustic shielding [25], as well as the position of the FOH under the sonotrode which influences the recorded pressure [22].

Supplementary video related to this article can be found at https://doi.org/10.1016/j.carbon.2022.12.070.

The visual observation of a large bubble cloud collapse in conjunction with a large spike can be seen for each tested solvent in Fig. 1 (the third image in the sequence). For each solvent the maximum area of the

developed cavitation zone was measured using the high-speed imaging. Salient observations from the DIW cavitation activity showed a localised primary cavitation cloud at the tip of the sonotrode, measured to be ~ 1.13 mm^2 in cross-section (Table S2) at 20% sonication power. The satellite bubbles underneath were small in size (65–250 μm maximum diameters, Table S2) and vigorously oscillated mostly in stable cavitation modes. In contrast, EtOH, DIW:EtOH and NMP all generated much larger cavitation zones. The cross-sections of the primary cavitation cloud formed under the sonotrode tip for EtOH, DIW:EtOH and NMP were measured to be ~ 3.19, 3.17 and 2.33 mm^2, respectively. As DIW has a significantly higher surface tension compared to the other solvents (Table S1), it is less likely to nucleate bubbles at such a low input power (20%); therefore, the primary cavitation cloud was expected to be smaller in size [20,26]. Tables S1 and 2 shows this trend in solvents with a decreasing surface tension producing a larger cavitation cloud. Additionally, the viscosity of the liquid medium influences the cavitation zone size. A larger viscosity can contribute to increasing the cavitation zone [27], hence, producing a larger cavitation zone formed under the sonotrode tip.

These tendencies were also observed for the secondary cavitation clouds produced by each solvent, with more satellite bubbles extending the overall cavitation spatial distribution. For instance, satellite bubbles generated in EtOH were measured to have diameters approximately twice the size of those in DIW at the same input power (Table S2). The larger primary and secondary cavitation zone formed under the sonotrode for NMP (coinciding with the proclivity for bubble collapse demonstrated by the large pressure spikes in Fig. 1(d)) is likely a contributing factor for its exfoliation efficiency. We have previously demonstrated using synchrotron X-ray phase-contrast imaging that the bubble density under the sonotrode for NMP was nearly twice that of DIW [28]. The synchronised imaging and pressure measurements provide additional evidence that the bubbles produced in NMP are more effective in terms of delamination of layered materials such as graphite.

It is important to note that despite producing a larger cavitation zone, or more bubbly clouds, larger acoustic pressures are not necessarily generated. Increased intensity of cavitation activity is determined by the level of detectable prominent peaks and SWs within the emission signal [23,25]. We can observe from Fig. 1 that during the initial period upon the sonotrode activation (<15 ms) ultrasound produced higher acoustic pressures than afterwards, when the primary cloud reached its stable size (the fourth image in the sequence). This short ultrasonic period giving rise to higher pressures makes a case for using pulsed ultrasound. The higher measured pressure amplitudes could be due to the phenomenon that pulsed ultrasound can promote nuclei replenishment, hence generating more cavitation and transient cavitation collapses detectible via the FOH [27,29]. Employing a short, powerful ultrasonic burst may be beneficial for a variety of applications such as preventing reactor clogging and reducing energy usage [30,31]. However, for ULPE, further testing would need to be conducted. The “pause” during deactivation of the sonotrode may decrease the time that flakes require to sufficiently exfoliate, as well as affecting sustained acoustic flow and recirculation.

The appearance of the cavitation activity for DIW was very different due to the reduced nucleated bubbly clouds. EtOH and NMP were similar (Video 2 & 3 in Supplemental materials), producing darker clouds demonstrating the larger area occupied by the bubbles. Interestingly, the addition of EtOH to the DIW significantly changed the appearance and bubble dynamics. Activation of the sonotrode was seen to generate “mist” of cavitation bubbles, producing an extended, very dark cavitation cloud (observed in Fig. 1(c) and Video 4). Due to the largely dispersive nature of the bubbles (where clouds appeared to be comprised of tiny cavitation bubbles spread out homogeneously, which made it difficult to distinguish between primary and secondary cavitation clouds), measuring the secondary cavitation cloud posed a problem. We can, however, suggest that this type of bubble dynamics may be more useful for exfoliating layered material by in-layer penetration, producing a gentler exfoliation as reported previously [14].

Supplementary video related to this article can be found at https://doi.org/10.1016/j.carbon.2022.12.070.

General observations from the data in Table S2 demonstrated that an increase in sonication power for each solvent generated a larger primary cavitation cloud. We observed DIW to show the greatest percentage increase in primary cavitation area, of ~ 270%, when changing sonication power (equivalent to the generator power) from 20 to 100%. Interestingly, the increase in acoustic power was less effective at generating a larger primary cavitation cloud for solvents with lower surface tensions (the increase measured as 82, 67, 45% for NMP, DIW:EtOH and EtOH, respectively).

Fig. 2 presents the measured acoustic pressures for each solvent using a larger sonotrode (Section 2.1) ideal for ULPE at scale, which was used for prolonged experiments in Section 3.2. A stabilised cavitation regime for the solvents revealed the same trend (as seen in Fig. 1). The highest recorded P_{RMS} pressures arose from NMP and DIW, followed by the DIW:EtOH mixture and EtOH (Fig. 2(a)). This observation once again confirms the effect of physical properties. NMP has a significantly lower vapour pressure than all the solvents under investigation (Table S1, ideal for more bubble collapse). This may explain the high acoustic pressures measured. However, the significantly higher surface tension of DIW (Table S1) promotes more powerful bubble implosions, hence, producing a larger number of SWs interacting with the FOH tip than in NMP. EtOH producing the lowest acoustic pressures can also be explained by the physical properties [25]. The cavitation strength is

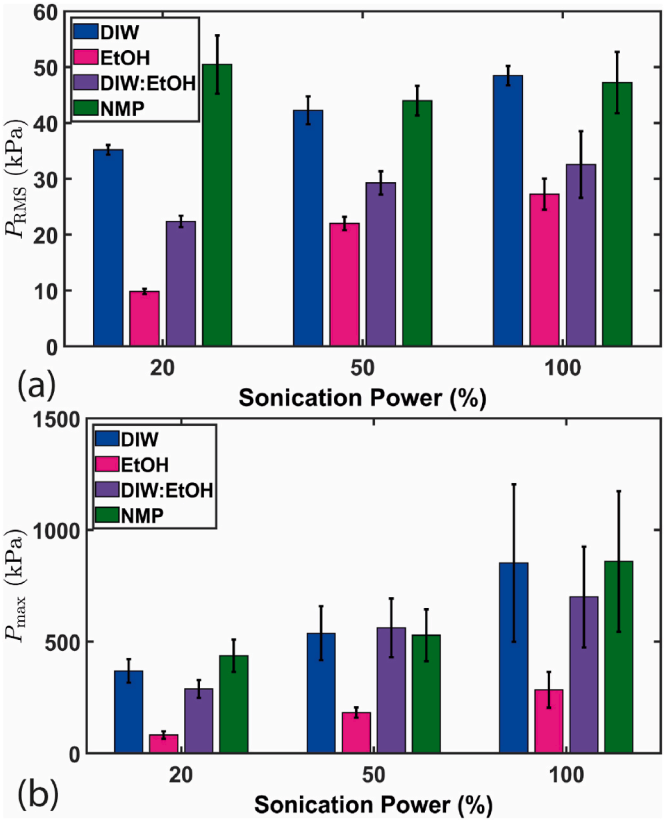

Fig. 2. Pressure measurements taken with the FOH for solvents under investigation; **(a)** P_{RMS}; **(b)** P_{max}. The acoustic intensity ($\times 10^{-4}$ W/m^2) corresponding to the sonication input powers are as follows: DIW; 9 (20%), 13 (50%), 37 (100%); EtOH; 3 (20%), 10 (50%), 30 (100%); DIWEtOH; 3 (20%), 17 (50%), 34 (100%); NMP; 8 (20%), 20 (50%), 40 (100%) (calculations in Table S4). Data was recorded from 60 waveforms of cavitating emission signals using a 2-ms time period, and averaged for each case (Section 2.1). The temperatures of the solvents were maintained at 40 °C. (A colour version of this figure can be viewed online.)

directly affected by the surface tension at the liquid-gas interface, as well as the initial bubble radius, therefore, we can also expect the large pressure difference between DIW and EtOH (having the highest and lowest surface tension, respectively). Due to the ability of EtOH to reduce cavitation bubble impact [32], we can hypothesise that a bulk-layered material exposed to repeated SWs (of smaller acoustic pressure, Fig. 2) would suffer lesser deleterious effects such as structural defects. EtOH has a significantly higher vapour pressure that promotes bubble formation but also impedes bubble implosion (Table S1) [25]. The mixture of DIW and EtOH was, in-part, proposed to balance generating sufficient SW impacts to exfoliate layered materials, as well as ensuring minimal surface damage. It has been previously reported that DIW as a liquid medium can induce defects due to the greater impact of SW interactions [19]. Lowering defects promotes production of pristine graphene, and would increase applicatory uses of the exfoliated nano-sheets. This defect reduction is also later confirmed in Section 3.2.

Before optimizing our experimental setup for ULPE at 40 °C, preliminary testing was also conducted at 20 °C. The acoustic pressure plots demonstrate the same trend for most of the solvents, albeit higher measured pressures at 40 °C (Fig. 2 & Fig. S3). Interestingly, NMP pressure measurements at 20 °C (Fig. S3) were significantly lower than those at 40 °C, and also in comparison to the temperature change in the other solvents. Some previous research has opted to use NMP at 40 °C during ULPE, without presenting specific, fundamental justification [33]. It is possible that from a physical perspective, increased cavitation activity facilitates of exfoliation at this temperature. A higher temperature solution can often increase the production of cavitation bubbles [34]. Non-dimensional analysis of NMP at both 20 °C and 40 °C revealed an increase in the Reynolds number (Table S3), indicating the temperature rise enhanced inertial forces leading to bubble collapses [25].

To our knowledge, this is the first time NMP has ever been investigated quantitatively in terms of acoustic pressure in conjunction with cavitation dynamics under ultrasound. The analysis of the data implies that NMP can produce strong cavitation that varies distinctly with temperature (Fig. 2 comparison with Fig. S3). NMP needs lesser agitation to break apart layered materials than other solvents, largely a consequence of its chemical properties (i.e. Hansen's solubility parameter) [35]. This research indicates the proclivity to exfoliate so effectively is a combination of chemical and physical properties, whereby cavitation bubbles play a larger role than previously thought. The higher temperature increases the number of these bubbles, hence, increasing the SW generation and aligns with our previous camera observations and measurements of the large cavitation zone for NMP at 40 °C. The introduction of ultrasound increases the exfoliation efficiency, in addition to assisting in the dispersion of material within the liquid medium (Section 3.2). Despite these benefits, due to the large acoustic pressures measured, the ultrasonic cavitation in this case may increase the chance for deleterious effects on the nano-sheets. It is also noteworthy to recall the hazardous and contaminating nature of NMP.

As SWs appear to be the primary mechanism to facilitate exfoliation of layered materials in DIW [14], we must also consider the P_{max} pressure (Fig. 2(b)). The calibration of the FOH (1–30 MHz) is primed to detect SWs, and the data on the maximum acoustic pressure assists our analysis to detect the role of SWs generated in each solvent (i.e. SWs generally induce the highest cavitation intensity). We observed that NMP, DIW and DIW:EtOH behave similarly, despite some variation due to sonication power. From our previous study, we have identified a moderate generator power (50%) to provide appropriate acoustic flow [36] in conjunction with the necessary cavitation intensity to promote exfoliation of graphite [20,21]. Interestingly, conditions set at 40 °C and at 50% input power demonstrated very similar acoustic pressure for NMP and DIW:EtOH in the range of 0.5 MPa (Fig. 2(b))). We could hypothesise from this data that these conditions may ensure exfoliation in DIW:EtOH through similar bubble dynamics and SW interactions as in NMP.

Another positive aspect of using DIW:EtOH may arise from an increased wettability. For the case of DIW (with the highest surface tension), a poor wettability with the source graphite leads to floating particles on the liquid surface (even when acoustic energy is introduced), therefore, promoting an inefficient use of the material. Additionally, a higher wettability for DIW:EtOH aids to disperse the layered material into the solvent, facilitating exfoliation as graphite particles can be re-circulated into the primary cavitation zone under an acoustic flow.

These data, along with the high-speed imaging are indicative that the combination of DIW:EtOH would be a promising candidate for ULPE. As previously mentioned, the surface tension of DIW is not ideal for stabilisation of exfoliated nano-sheets, therefore, re-agglomeration occurs over short periods. Due to the DIW:EtOH mix decreasing the surface tension disparity between DIW and NMP (considered to have close to optimum surface tension for exfoliating graphene) we can hypothesise that the exfoliated material suspension would remain stable, and in turn increase the yield (as later demonstrated in Section 3.2 Fig. 4(c) and (d)). Furthermore, we suggest that due to the increase in size of the cavitation zone (Fig. 1), the localisation of cavitation would pose less of an issue, and lead to increased layered material exfoliation throughout the liquid medium due to extended shearing forces introduced via larger and more distributed satellite bubbles and cavitation bubble "mist". Finally, due to the size of cavitation "mist" bubbles induced within the DIW:EtOH mix, a gentler exfoliation may be promoted (similar to the high-frequency (~1.2 MHz) exfoliation mechanism [19]) with these cavitation bubbles fitting in-between inner flake layers, hence, reducing structural defects whilst expediting layer delamination.

Therefore, the use of the high-speed camera that proved to be a beneficial tool for this study revealed the behaviour of bubbles in the studied liquids with different properties. For example, it is shown that bubbles in EtOH with low surface tension coalesce and generate large bubbly structures with less tendency to collapse (also indicated by the pressure waveform in Fig. 1). However, bubbles in DIW:EtOH with a surface tension closer to NMP and higher viscosity produce a stable "mist" of bubbles that has been previously identified in Ref. [32] as a potential mechanism to enhance exfoliation via the interaction with partially exfoliated graphene flakes as predicted in Ref. [14]. High quality exfoliation using DIW:EtOH was later confirmed by the outcomes of this study (Section 3.2).

3.1.2. *Shadowgraphic ultra-high-speed imaging*

Although the analysis on the bubble dynamics in conjunction with synchronised acoustic pressure measurements gave us some indication as to the mechanisms through which sonication in different solvents may affect exfoliation, more specific features of this exfoliation can be analysed through detailed observation of SW generation and propagation for each solvent. Previous research from our group had demonstrated SW analysis from the perspective of acoustic spectra [22,32], however, to gain a better insight shadowgraphic photography was utilised to evaluate the evolution and propagation of SWs in real-time. This was taken as a pre-condition experiment before we undertook ULPE for extended durations (Section 3.2). Fig. 3 shows representative, *in situ* image sequences of SW generation with varying input power for each tested solvent.

In the duration of 255 μs of sonication (corresponding to ~ 6 acoustic cycles) we registered the solvents to produce six "bursts" of SWs, i.e. multiple SWs generated upon collapse of the primary cavitation cloud. These bursts were fairly periodic and hence, bubble clouds were collapsing harmonically consequently to the sonotrode operational frequency (24 kHz). Despite the number of these bursts remaining constant irrespective of the liquid medium, the duration of the release of SWs, as well as the approximate number of generated SWs varied with the sonication power and solvent (Videos 5-8). We observed that an increase in sonication power generally produced more SWs. Fig. 3 displays this tendency with the number of visible SWs increasing from images 1

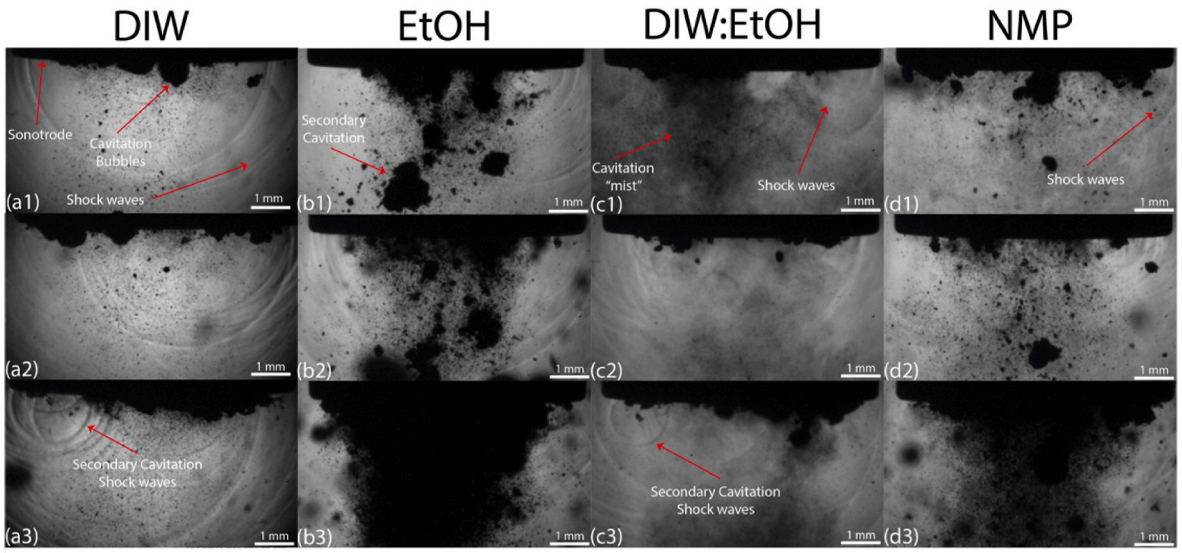

Fig. 3. Shadowgraphic images showing representative frames of SW generation for solvents; **(a)** DIW, **(b)** EtOH, **(c)** DIW:EtOH and **(d)** NMP. Sequences 1–3 show an increasing generator power of 20, 60 and 100%, respectively. (A colour version of this figure can be viewed online.)

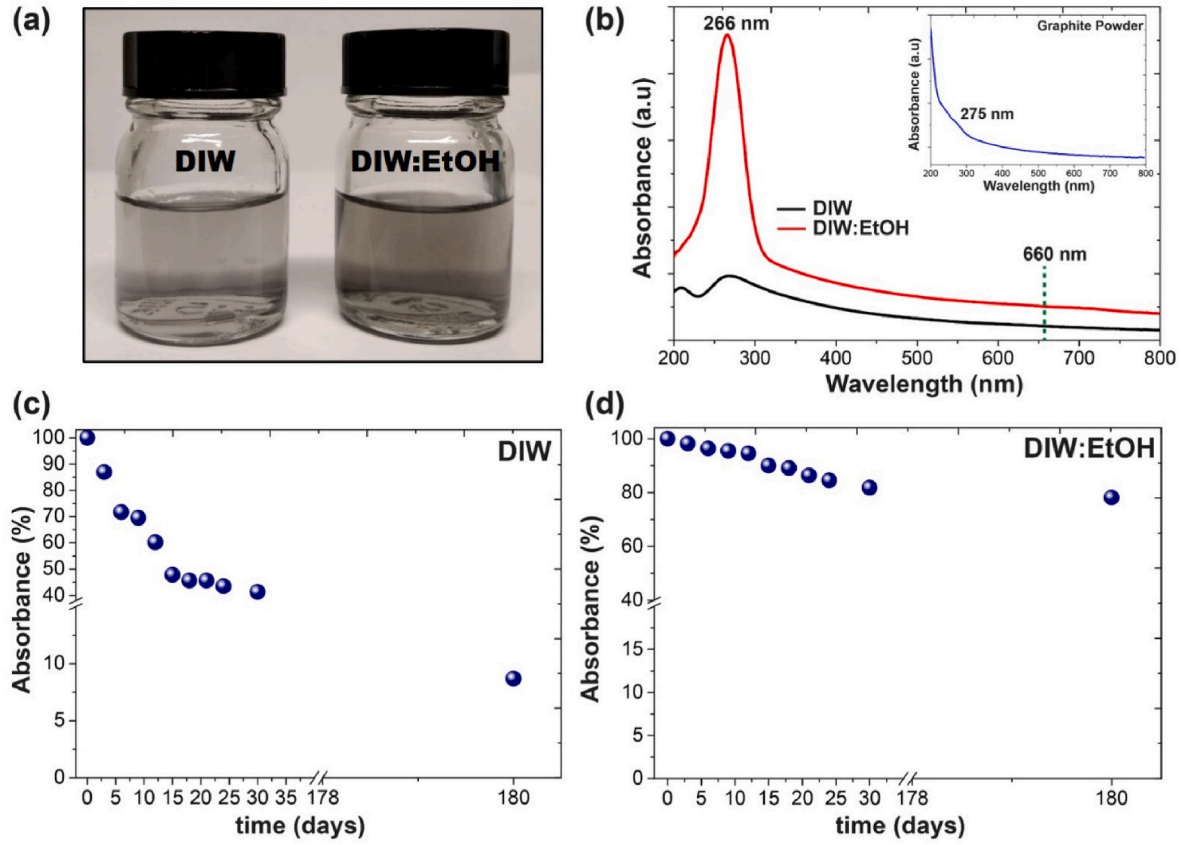

Fig. 4. **(a)** Photograph of obtained supernatants in DIW and DIW:EtOH post sonication-centrifugation process. **(b)** UV–Vis spectra of obtained supernatants. The inset displays a UV–Vis spectrum of the starting material GP. **(c)** & **(d)** sedimentation plots of graphene suspension in DIW and DIW:EtOH, respectively. (A colour version of this figure can be viewed online.)

through 3. We observed additional SW generation particularly for DIW (Fig. 3(a)) with increasing the power to 100%. However, it was also evident from the imaging that using 100% power could heavily supress some SW bursts due to the larger induced primary cavitation cloud (i.e. shielding effect) [37,38]. This was especially evident for EtOH (Fig. 3 (b3)) where the large extended cavitation cloud failed to collapse entirely, and hence, SW propagation was impeded by subsequent portions of the cavitation cloud which did not collapse. Although DIW:EtOH also produced an expanded cavitation cloud compared to pure DIW, the proclivity of the cavitation bubbles to collapse was greater than EtOH. The smaller "mist" cavitation enabled the propagation of SWs more freely (Fig. 3(c3)), similar to DIW. This appears consequentially of the

dark and opaque large aggregated bubble clouds observed in EtOH, as opposed to the light and transparent nature of the "mist", with tiny dispersed bubbles in DIW:EtOH.

Supplementary video related to this article can be found at https://doi.org/10.1016/j.carbon.2022.12.070.

Calculating SW velocities for each solvent using the high-speed image sequences revealed no change with sonication power as expected [22]. All the solvent SW velocities were in the range of 1400–1550 ms^{-1} with the exception of EtOH, generating lower velocities between 1100 and 1200 ms^{-1}. This correlates to the known speeds of sounds for these liquids (e.g EtOH is ~1100 ms^{-1} [39–41]. These weaker generated SWs are likely a contributing factor as to the lower recorded acoustic pressures for EtOH (Fig. 2).

Our group has previously investigated the frequency spectra related to SW generation for DIW [22] and EtOH and DIW:EtOH [32]. The findings for DIW revealed a characteristic pressure peak at ~3.3 MHz predominantly generated via SWs. Interestingly, further results identified this peak for DIW:EtOH. Our analysis revealed that NMP also produced this inherent SW peak (Fig. S4), additionally confirming that transient cavitation is a prominent feature in NMP that aids exfoliation (consistent with generating large SW-induced peaks in Fig. 1(d) and large P_{max} pressures in Fig. 2(b)), in addition to its chemical properties. However, for EtOH, this SW-induced pressure peak was only generated at higher sonication powers indicating suppressed transient bubble collapses, whereby shielding decayed the SW impact before its interaction with the FOH (aligning with EtOH's physical properties). The data also corresponds with the lower measured acoustic pressure for EtOH (Fig. 2), along with the lower propagation speed of SWs throughout the medium.

All solvents were seen to produce SWs close to the sonotrode tip. Despite a larger number of secondary cavitation bubbles formed by EtOH, they demonstrated fewer transient collapses, in addition to having oscillations of reduced amplitude. For the case of DIW, secondary cavitation collapses appeared to occur more frequently (Fig. 3(a3)), demonstrating the solvent capability to generate higher acoustic pressures. This property was also noticeable for DIW:EtOH (Fig. 3(c3)). It is possible that due to the heightened ability to produce secondary cavitation (adopted through the addition of the EtOH) in a "mist" cloud formation (as discussed in 3.1.1), DIW:EtOH may work as a more efficient exfoliator, able to shear layers of flakes at further distances from the sonotrode tip. This hypothesis was tested in the next section.

3.2. Ultrasonic exfoliation of graphite & its characterisation

Following the investigation of cavitation activity and bubble dynamics for each solvent, analysis could now be carried out to determine the benefits of using DIW:EtOH as an eco-friendly liquid medium for ULPE. The experiments were conducted using the optimized ultrasonication parameters based on previous research (and as identified in Section 2 of Appendix A in the Supplementary); a sonication power of 50% and solution [19–21] temperature of 40 °C over a 2 h sonication period.

The scope of this study was to focus on eco-friendly liquids as a viable alternative to NMP; hence, we chose not to carry out our own NMP ULPE experiments. Our recent study [18] investigating LPE in NMP was carried out to compare the exfoliation efficiencies and dispersibilities of eco-friendly solvents under investigation such as (DIW), Isopropyl alcohol (IPA), EtOH, DIW:EtOH etc. with NMP. Interestingly, the findings of this work suggest that the exfoliation efficiencies of both IPA and EtOH, exceeds that of NMP for GR150 (Graphite flakes, 100 mesh) whereas for GR50 (Graphite powder, 300 mesh), the exfoliation efficiencies of IPA and EA (Ethyl Acetate) are comparable to that of NMP, which makes the robust case of utilising and harnessing the potential of eco-friendly solvents as opposed to toxic NMP. In addition, flakes exfoliated in NMP are highly defective with D/D' ratio ~4.5, indicating NMP improves the dispersibility and yield (0.40 ± 0.05 mg/ml) at the expense of producing disordered graphene flakes. In addition to the toxicity, NMP has a high boiling point (202 °C) which is challenging to remove after LPE, therefore resulting in degradation of material quality, and is well documented in the literature [42]. Hence, for all the aforementioned reasons ULPE in NMP was not conducted. However, for comparison purposes with this work we have also provided information on the exfoliation degree, yield, quality and stability of graphene in NMP, as documented by other researchers in Table S5 in the Supplementary Section.

3.2.1. UV–visible spectral analysis

Fig. 4(a) and (b) demonstrate obtained supernatants post sonication for 2 h followed by centrifugation at a relative centrifugal force (RCF) of 1500 *g* as explained in Section 2.1 of Appendix B in the Supplementary and their recorded UV–Vis absorption spectra for DIW and DIW:EtOH, respectively. From the spectra, the absorption peak around ~266 nm certifies the graphene characterstics, pertaining to π-π* transitions of C═C sp^2 bonds [43]. In respect of the absorption spectrum of precursor graphite powder (GP) (as shown in inset of Fig. 4(b)), it appeared that the successful exfoliation of graphene had been achieved in both the samples. Crucially, incidence of a prominent and sharp peak in the DIW:EtOH sample advocates the enhanced degree of exfoliation, dispersion-uniformity and the likelihood of few layer graphene (FLG) flakes, while the DIW sample gave imprints of polydisperse behaviour [43]. From Fig. 4(b), it was evident that the concentration of graphene flakes (qualitative estimate of concentration i.e. A/ℓ as per Lambert–Beer's law, A/ℓ (at 660 nm) = αC where A is measured absorbance, ℓ is optical path length, α is extinction coefficient and C is concentration of dispersion [9]) was found to be higher in DIW:EtOH in contrast to the DIW sample as indicated with the dotted line. For a quantitative insight, yield estimations for the produced graphene were carried out based on the experimental investigations. It was established that exfoliation in DIW:EtOH produced a yield twice that of DIW at 1200–1500g (see Section 2.4 in the Supplementary for further details).

To investigate the stability of suspensions, sedimentation curves were plotted with the progression of time, which are displayed in Fig. 4 (c) and (d). The term "Stability" can be defined as the amount of retained graphene in the supernatant over a period of time, which has also been considered as a relative measure of the ability of the solvent to stabilize the graphene suspension. This amount was estimated by recording the absorbance of the suspension at a wavelength of 660 nm (as per Lambert–Beer's law), followed by its normalization and conversion to percentage [44]. The sedimentation plots revealed that graphene dispersed in DIW:EtOH exhibited improved stability; ~81% and 78% of graphene remained suspended after one and six months, respectively, whilst for DIW, only ~40% and 8% after one and six months, respectively. These data clearly suggest the addition of EtOH to DIW played a significant role in stabilizing the graphene dispersion.

3.2.2. Raman spectral analysis

Raman spectroscopy was deployed for characterization of the graphene flakes produced by sono-exfoliation in the solutions under investigation, which provides information on a variety of their properties ranging from defect density, layer-count and evidence of exfoliation [45]. Fig. 5 (a) depicts the Raman spectra of representative graphene flakes found in DIW and DIW:EtOH, establishing characteristic signatures of graphene, i.e. D, G, D' and 2D bands. The spectra are labelled as single-layer graphene (SLG), bi-layer graphene (BLG) and FLG in accordance with their intensity ratios (I_{2D}/I_G) which is discussed comprehensively below. The D and D' bands centred on ~1350 cm^{-1} and 1620 cm^{-1} respectively manifest the structural defects in sheets arising due to disruption in regular aromatic sp^2 networks that are so called non-sp^2 or sp^3 defects [45]. The G peak at ~1580 cm^{-1} governs in-plane motion of sp^2 bonded carbon atoms together with its upshift towards higher wavenumbers indicating both disorder in regular structure and increasing sheet thickness [45]. Finally, the 2D peak

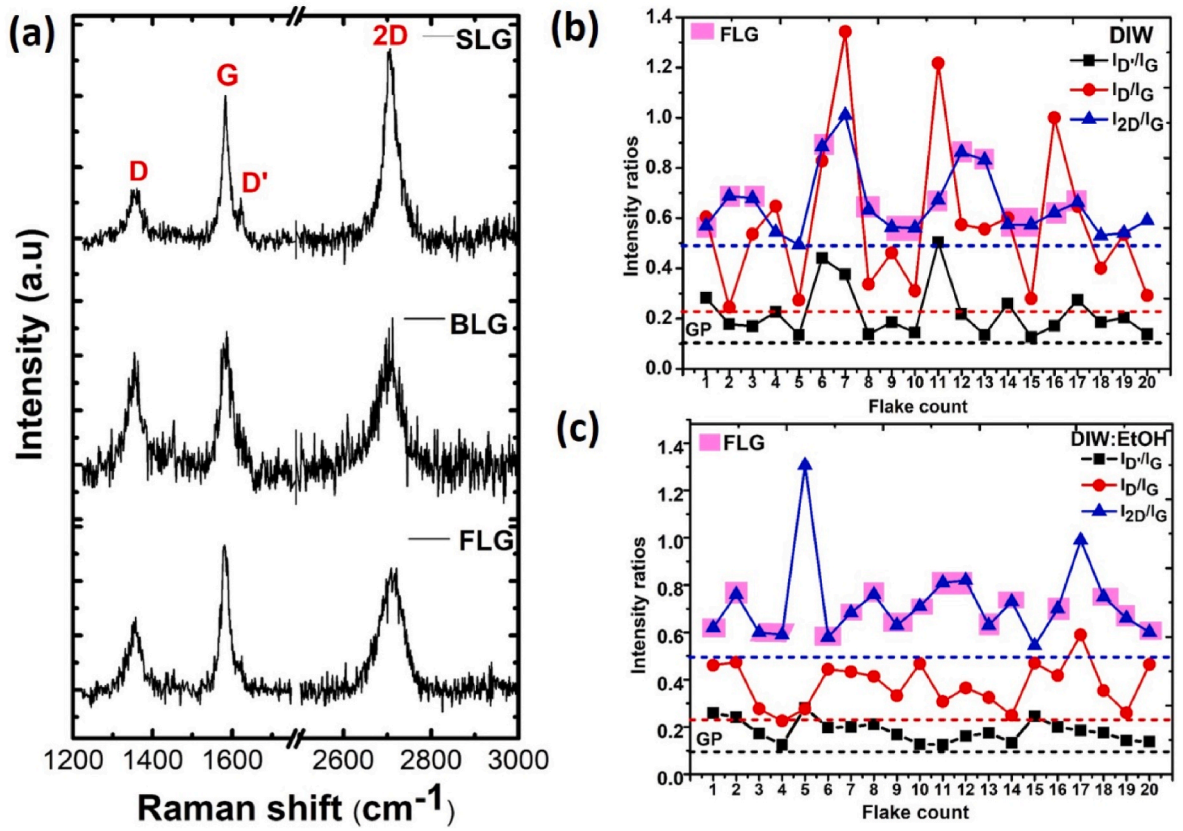

Fig. 5. **(a)** Representative Raman spectra (normalized to the G-band intensity) of SLG, BLG and FLG found in DIW and DIW:EtOH featuring the characteristic signals of graphene: D, G and 2D bands. The spectra are labelled SLG, BLG and FLG in accordance with I_{2D}/I_G intensity ratios (note SLG was only found in the DIW:EtOH samples). **(b)** and **(c)** highlight intensity ratios ($I_{D'}/I_G$ (black squares), I_D/I_G (red spheres) and I_{2D}/I_G (blue triangles) of graphene related peaks found in DIW and DIW:EtOH, respectively. Each point corresponds to parameters extracted from an individual spectrum of a registered flake. Intensity ratios for the original GP are shown by the dashed lines of the same colour as data for intensity ratios. (A colour version of this figure can be viewed online.)

around ~2720 cm^{-1} features a second-order overtone of in-plane vibration of the D band [46]. Principally, the variations in line-shape, intensity, peak-position and width of the 2D band reveal information related to the number of graphene layers [45,46]. To serve this purpose, the qualitative layer-count estimations can be accomplished by performing Lorentzian fitting to the 2D band for its deconvolution into sub-peaks. For SLG, the Raman 2D band can be fitted with only single Lorentzian peak with full width half maximum (FWHM) ~24-30 cm^{-1} which arises due to the single electronic excitation between π valence band and π* conduction band [47]. It is evident from Refs. [45–47] that the FWHM of the 2D band widened with an increase in number of layers. For the case of FLG, due to π-electron interaction under AB stacking, the electronic bands split into dispersive configurations allowing more resonant phonons with diverse frequencies which contribute, to both widening and lowering of the 2D band intensity [48]. Another important parameter is the ratio of intensity of 2D to G band i.e. I_{2D}/I_G whose values reflect the variation in the number of layers [46–48].

It is critical to assess the quality of the obtained exfoliated graphene sheets. According to studies of Ferrari et al. [46], defect stages can be monitored by estimating the FWHM of the G band which states that a higher degree of disorder corresponds to a broader G band. Furthermore, another significant parameter is the defect ratio, i.e. ratio of the intensity of the D band to G band (I_D/I_G), which is a quantitative index and can also be employed to gauge the degree of disorder in carbon based materials. For a better understanding, it is of great importance to investigate the nature of defects whether basal plane or edge defects. Nevertheless, the existence of edge defects is unavoidable as the ultra-sonication process induces reduction in flake sizes through fragmentation. Additionally, the ratio of intensity of the D′ band to G band, i.e. $I_{D'}/I_G$ furnish information related to the presence of edge defects in crystal structure [47,48].

Based on the above-mentioned criteria, parameters such as defect ratio I_D/I_G (red dots), $I_{D'}/I_G$ (black squares), I_{2D}/I_G (blue triangles) had been extracted from each recorded spectrum and plotted in Fig. 5(b) and (c) for graphene flakes found in DIW and DIW:EtOH, respectively. It should be noted that each point corresponds to the parameters extracted from a recorded spectrum, corresponding to a Raman spectrum of an individual flake under investigation. Graphene sheets in the DIW:EtOH sample were constantly falling within the low defect regime (I_D/I_G ~ 0.23–0.58) in comparison to the DIW sample which demonstrated a more erratic behaviour (I_D/I_G ~ 0.24–1.34). This consistency and reduced variation in the defect ratios of DIW:EtOH also reflects the homogeneity of dispersed graphene flakes. The increased I_D/I_G intensity ratio likened to the original GP (as indicated with the dashed line in both Fig. 5(b) and (c)) is understandable in terms of incorporation of defects resulting from a thinning of graphite after LPE processing. In addition, $I_{D'}/I_G$ ratios for graphene in DIW posed a rather wider range of ~0.12–0.51 in contrast to DIW:EtOH with a narrower range of ~0.13–0.25, indicating less defective exfoliated sheets in DIW:EtOH. Moreover, I_{2D}/I_G ratios of ~0.55–1.01 and ~0.60–1.30 corroborate the formation of FLG sheets in DIW and DIW:EtOH, respectively, with apparent SLG signatures (I_{2D}/I_G ~ 1.3) found in the DIW:EtOH sample. It is evident from Fig. 5(b) and (c) that the majority of registered flakes are in the range of FLG with identification of few SLG and BLG graphene signatures (I_{2D}/I_G ~ 1) accompanied by sheets displaying a more consistent pattern across all the intensity ratios in DIW:EtOH. However, BLG signatures were also found in DIW samples. It can also be deduced from the above observations that the presented processing technique

works well for the systematic production of FLG.

For further clarity, the correlation between the defect ratio (I_D/I_G) and FWHM of the G band have been plotted in Fig. 6(a). From the graph, it was observed that values of FWHM of the G band are densely populated in the range of 20–25 cm^{-1} for DIW:EtOH, while for DIW there is a sparse variation of FWHM ranging from 20 to 45 cm^{-1}, which might be due to instigation of bulk defects in some flakes coupled with edge defects.

In other words, both the range of defect ratios and the relatively reduced broadening range of the G band in the DIW:EtOH sample constitute persuasive evidence that defects induced in sheets are attributable to the edge defects rather than basal defects. However, in the DIW sample with I_D/I_G ratios of 0.24–1.34, there are some flakes for which the I_D/I_G ratio exceeded 1, possibly suggestive of basal defects, or alternatively an indication of the fineness of flakes. For a deeper analysis, another crucial parameter, i.e. the ratio of intensity of the D band (I_D) over D′ band ($I_{D'}$), has been evaluated and plotted in Fig. 6(b) to verify the nature of those defects. In accordance with Eckmann et al. [49], $I_D/I_{D'}$ ratios of ~13, ~7 and ~3 indicate the presence of sp^3 defects, vacancy defects and edge defects, respectively. From Fig. 6(b), $I_D/I_{D'}$ values of less than 3.5 were found (highlighted with the yellow shaded area) which indicated the presence of edge defects rather than basal defects in graphene sheets obtained in both DIW and DIW:EtOH.

To obtain quantitative information about the layer-count, Eq. (4) suggested by Backes et al. [43] was employed and the graph of I_{2D}/I_G versus number of layers is depicted in Fig. 6(c). The graph illustrates that the majority of layer-count values are located within 3–5 layers (highlighted with the yellow shaded area), associated with FLG sheets. Results are also in accordance with [19] where a similar technique demonstrated that FLG in the range of 3–5 layers thick were systematically produced in sonicated water.

$$<N \geq 1.04 \times M^{(-2.32)} \quad (4)$$

where <N> is the average number of layers per sheet and M is I_{2D}/I_G.

Histogram data (Fig. 6 (d)) revealed that the majority of registered flakes in DIW and DIW:EtOH were FLG (3–5 Ls). However, the maximum population of thinner flakes were found in DIW:EtOH. In order to further validate the above-mentioned argument, deconvolution of the 2D peaks was performed using a Lorentzian fitting ($R^2 \sim 0.98$–0.99) after applying a linear baseline subtraction to obtain qualitative information of layer-count, and representative fitted curves (given in Fig. B7 (a) and (b), Section 2.4 of Appendix B in the Supplementary file). From the deconvolution graphs, sub-components of the 2D band were found suggestive of FLG in both DIW and DIW:EtOH. The average values of I_D/I_G, $I_{D'}/I_G$, I_{2D}/I_G, $I_D/I_{D'}$ identified from Raman measurements for the investigated flakes in DIW and DIW:EtOH are provided in Fig. 9. To summarise, Raman results showed the existence of FLG sheets in both DIW and DIW:EtOH, with exfoliation in DIW:EtOH giving somewhat thinner and higher quality flakes. High-resolution microscopic techniques have been further conducted for validation.

3.2.3. Morphological analysis

To assess the quality and size-metrics of the obtained graphene flakes after ULPE, TEM investigations were performed. Fig. 7(a–c) gives representative TEM images of graphene sheets exfoliated in DIW with Fig. 7(c) indicating measurements of length, <L> and width <W>. It should be noted here that flakes that have a visible outline have been considered for dimensional analyses. Some of the recorded images exhibit folded and wrinkled regions which can be assumed as the intrinsic nature of graphene sheets after ULPE [50].

Fig. 7(e–g) feature representative TEM images of graphene sheets dispersed in DIW:EtOH. For measurement accuracy the area of each flake had been exemplified in Fig. 7(d, h). High-resolution TEM (HR-TEM) images were recorded to estimate the layer-count by means of the edge counting method [51] as clarified in Fig. 7(i–l). Correspondingly, layer-count has been confirmed from respective plot profile diagrams

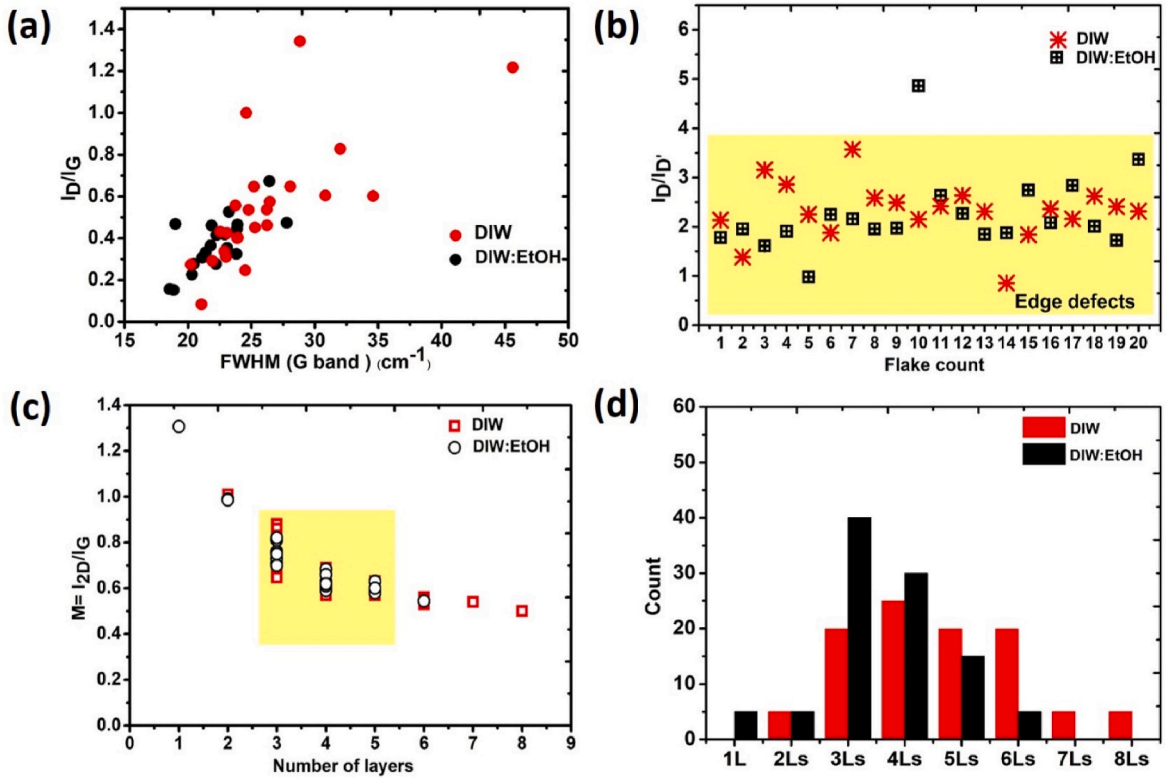

Fig. 6. **(a)** Plot of defect ratio (I_D/I_G) vs FWHM of the G band. **(b)** $I_D/I_{D'}$ ratios for investigated flakes confirming edge defects. **(c)** Co-relation between mean I_{2D}/I_G intensity ratios (M) as a function of layer number. **(d)** Histogram showing layer-count distribution in DIW and DIW:EtOH, respectively. (A colour version of this figure can be viewed online.)

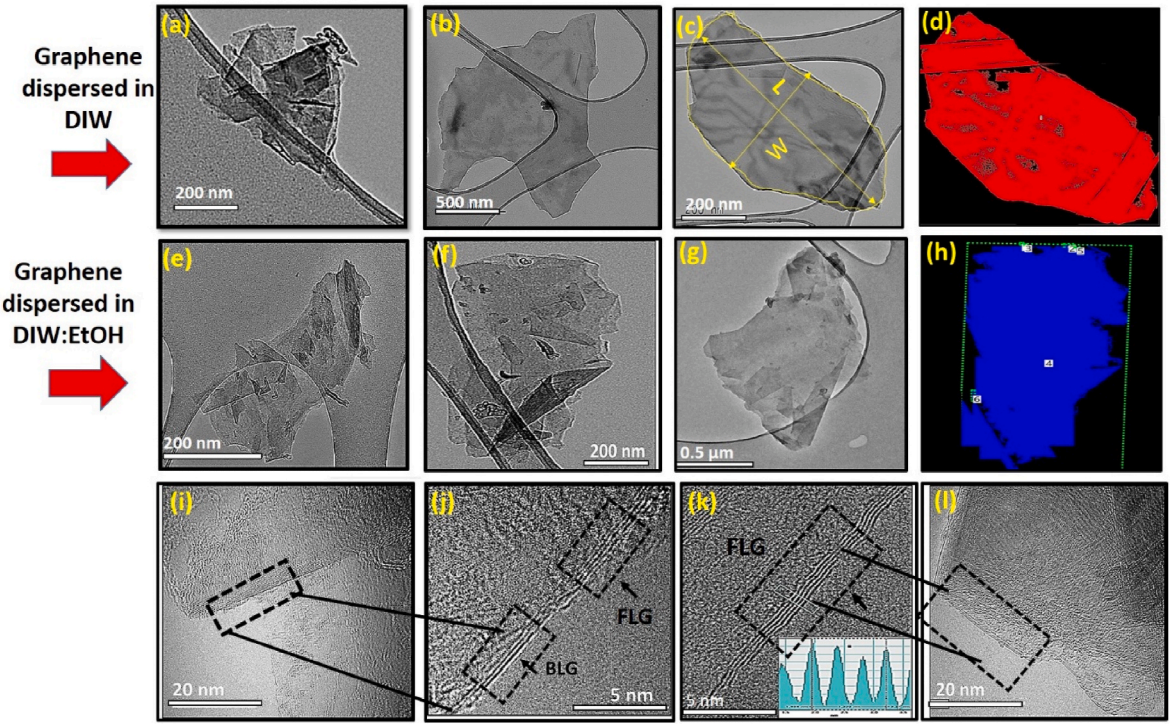

Fig. 7. **(a–c)** Representative TEM images of graphene sheets exfoliated in DIW, indicating measurement of average length (<L>) and width (<W>). **(d)** & **(h)** Illustrative measured area of investigated flakes designated with coloured regions. **(e)–(g)** Representative TEM images of graphene flakes exfoliated in DIW:EtOH. **(i)–(l)** HR-TEM images of examined FLG flakes (highlighted with black dotted rectangles). The inset of **(k)** displays a plot-profile of the highlighted portion, indicative of interlayer distances and layer-count performed using *ImageJ* software. (A colour version of this figure can be viewed online.)

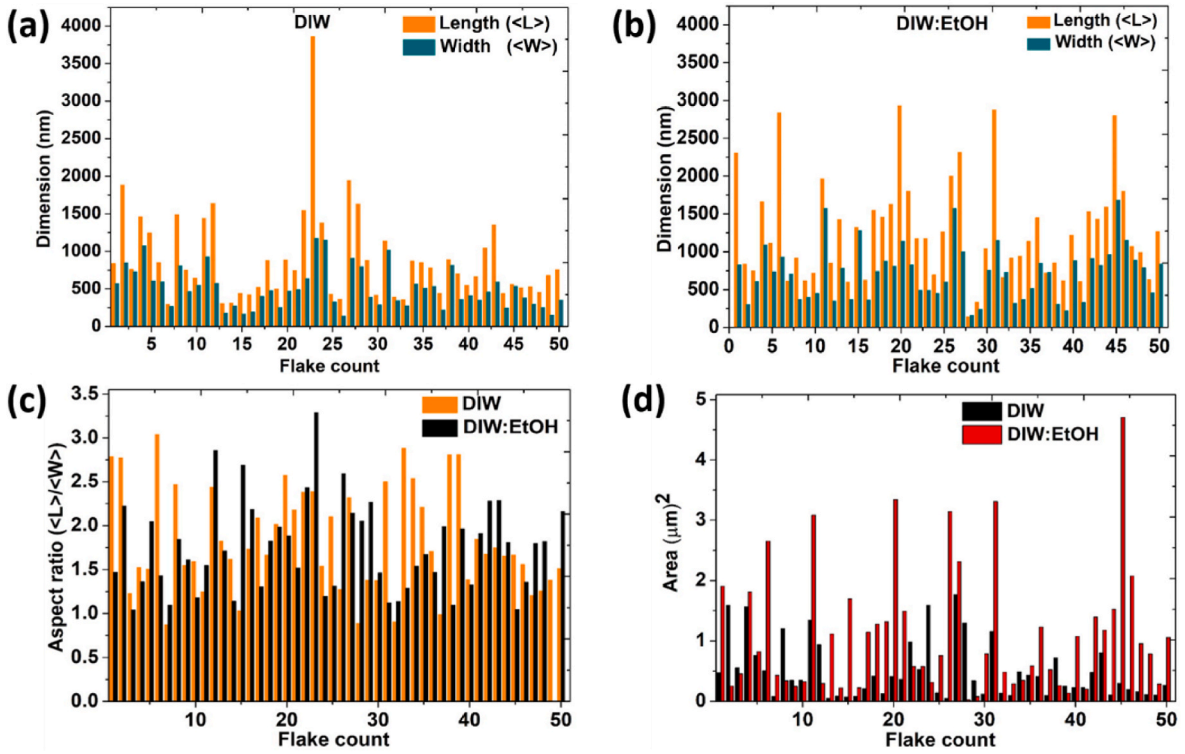

Fig. 8. **(a), (b)** Statistical histograms for dimensional analyses of observed 50 graphene flakes found in DIW and DIW:EtOH, respectively. **(c)** Statistical histogram showing mean aspect ratios (<L>/<W>) of the investigated flakes. **(d)** Statistical histogram of observed flakes for area measurements. (A colour version of this figure can be viewed online.)

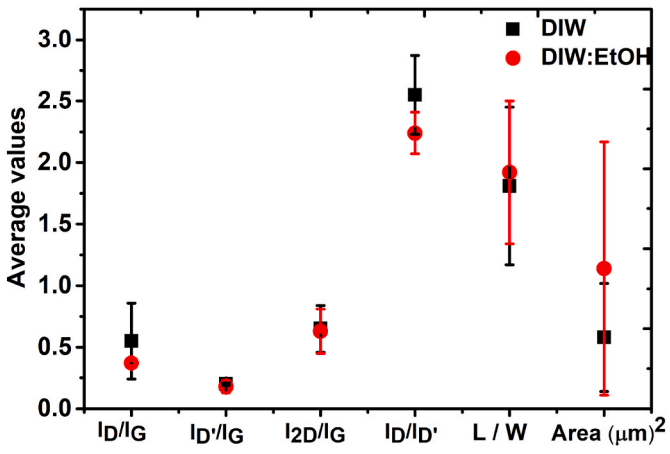

Fig. 9. The average values of I_D/I_G, $I_{D'}/I_G$, I_{2D}/I_G, $I_D/I_{D'}$, L/W and Area (with error margins) identified from Raman and TEM studies for the interrogated graphene flakes observed in both DIW and DIW:EtOH. (A colour version of this figure can be viewed online.)

(using *ImageJ software)* given in the inset of Fig. 7(k).

Statistical data from the recorded set of TEM images of the exfoliated graphene nanosheets was generated (Fig. 8). Fig. 8(a) and (b) demonstrate statistical analysis for the average values of length (<L>) and width (<W>) for the investigated graphene sheets found in DIW and DIW:EtOH, respectively. These data reveal the formation of FLGs several microns in cross-section and several μm^2 in area after ULPE in DIW:EtOH. Fig. 8(c) features the estimations of the mean aspect ratios (<L>/<W>) of flakes which are found to be in the ranges of 1.04–2.85 and 1.03–3.28 for DIW and DIW:EtOH, respectively. <L>/<W> $\neq$ 1 suggests the formation of elongated flakes which is a typical feature of LPE graphene flakes. Therefore, our TEM studies demonstrate the production of large sized graphene sheets in DIW:EtOH, fortifying the fact that the size of FLG flakes depends upon the nature of the dispersing medium, which in turn, controls both exfoliation efficiency and stability of flakes [16]. Fig. 8(d) advocates the occurrence of large sized graphene sheets in DIW:EtOH (area ~0.02–4.70 $(\mu m)^2$) as compared to DIW (area ~0.07–1.76 $(\mu m)^2$). Fig. 9 features the average values of parameters I_D/I_G, $I_{D'}/I_G$, I_{2D}/I_G, $I_D/I_{D'}$, L/W and Area $(\mu m)^2$ identified from Raman and TEM measurements for interrogated graphene flakes found in DIW and DIW:EtOH. From the statistical information related to the lateral sizes of graphene sheets recorded by TEM (see Fig. B8 in section 2.4 of the Supplementary material), we can deduce that the population of large sized graphene sheets, i.e. for the range of 500–1000 nm in DIW:EtOH is ~66% higher in comparison to DIW.

4. Conclusions

This study presents the first in-depth analysis comparing fundamental physical properties and *in situ* observations of bubble dynamics for a range of solvents used for ULPE, including NMP (currently most commonly used efficient solvent for exfoliation of graphene). Through the combination of high-speed imaging synchronised with acoustic pressure measurements recorded via a FOH, in conjunction with high-speed shadowgraphic imaging elucidating SW generation, a promising eco-friendly substitute (DIW:EtOH) was identified. ULPE for 2 h was carried out at various input powers for DIW and DIW:EtOH with resultant flakes analysed using a range of characterisation techniques. The mixture of DIW and EtOH was shown to produce higher quality few layer (3–5) graphene with a yield twice that of DIW, average flake area (~1.15 μm^2) and reaching a stability of ~78% for the duration of six months. Future developments will include further optimisation of experimental parameters and upscaling of the ULPE process.

Data availability

The data that supports the findings of this study are available upon request from the corresponding author.

CRediT authorship contribution statement

Justin A. Morton: Investigation, Conceptualization, Methodology, Writing – original draft, Visualization. **Amanpreet Kaur:** Writing – original draft, Investigation, Conceptualization. **Mohammad Khavari:** Investigation, Software. **Anastasia V. Tyurnina:** Investigation, Writing – review & editing. **Abhinav Priyadarshi:** Investigation. **Dmitry G. Eskin:** Writing – review & editing, Funding acquisition. **Jiawei Mi:** Writing – review & editing, Funding acquisition. **Kyriakos Porfyrakis:** Funding acquisition. **Paul Prentice:** Investigation, Writing – review & editing. **Iakovos Tzanakis:** Conceptualization, Writing – review & editing, Supervision, Funding acquisition.

Declaration of competing interest

The authors declare that they have no known competing financial interests or personal relationships that could have appeared to influence the work reported in this paper.

Acknowledgements

This work has been funded by the UK Engineering and Physical Sciences Research Council (EPSRC), to the project "Sustainable and industrially scalable ultrasonic liquid phase exfoliation technologies for manufacturing 2D advanced functional materials" (EcoUltra2D), with the grant nos. EP/R031665/1; EP/R031401/1; EP/R031819/1; EP/R031975/1.

Appendix A. Supplementary data

Supplementary data to this article can be found online at https://doi.org/10.1016/j.carbon.2022.12.070.

References

[1] K.S. Novoselov, et al., Electric field in atomically thin carbon films, Science 306 (5696) (2004) 666–669, https://doi.org/10.1126/science.1102896.
[2] A.K. Geim, Graphene: status and prospects, Science 324 (5934) (2009) 1530–1534, https://doi.org/10.1126/science.1158877.
[3] A.A. Balandin, et al., Superior thermal conductivity of single-layer graphene, Nano Lett. 8 (3) (2008) 902–907, https://doi.org/10.1021/nl0731872.
[4] K.I. Bolotin, et al., Ultrahigh electron mobility in suspended graphene, Solid State Commun. 146 (9–10) (2008) 351–355, https://doi.org/10.1016/j.ssc.2008.02.024.
[5] H. Tao, Y. Zhang, Y. Gao, Z. Sun, C. Yan, J. Texter, Scalable exfoliation and dispersion of two-dimensional materials-an update, Phys. Chem. Chem. Phys. 19 (2) (2017) 921–960, https://doi.org/10.1039/c6cp06813h.
[6] Z. Sun, Q. Fan, M. Zhang, S. Liu, H. Tao, J. Texter, Supercritical fluid-facilitated exfoliation and processing of 2D materials, Adv. Sci. 12 (1) (2019) 1–34, https://doi.org/10.1002/advs.201901084.
[7] K. Khan, et al., Recent developments in emerging two-dimensional materials and their applications, J. Mater. Chem. C 8 (2) (2020) 387–440, https://doi.org/10.1039/c9tc04187g.
[8] V. Nicolosi, M. Chhowalla, M.G. Kanatzidis, M.S. Strano, J.N. Coleman, Liquid exfoliation of layered materials, Science 340 (6139) (2013), https://doi.org/10.1126/science.1226419.
[9] Y. Hernandez, et al., High-yield production of graphene by liquid-phase exfoliation of graphite, Nat. Nanotechnol. 3 (9) (Aug. 2008) 563–568, https://doi.org/10.1038/nnano.2008.215, 2008 39.
[10] K.R. Paton, et al., Scalable production of large quantities of defect-free few-layer graphene by shear exfoliation in liquids, Nat. Mater. 13 (6) (Apr. 2014) 624–630, https://doi.org/10.1038/nmat3944, 2014 136.
[11] X. Gu, et al., Method of ultrasound-assisted liquid-phase exfoliation to prepare graphene, Ultrason. Sonochem. 58 (Nov. 2019) 104630, https://doi.org/10.1016/J.ULTSONCH.2019.104630.
[12] Y. Xu, H. Cao, Y. Xue, B. Li, W. Cai, Liquid-phase exfoliation of graphene: an overview on exfoliation media, techniques, and challenges, Nanomaterials 8 (11) (2018) 942, https://doi.org/10.3390/nano8110942.

[13] A. Tyurnina, et al., Ultrasonic exfoliation of graphene in water: a key parameter study, Carbon N. Y. 168 (2020) 737–747, https://doi.org/10.1016/j.carbon.2020.06.029.
[14] J.A. Morton, et al., New insights into sono-exfoliation mechanisms of graphite: in situ high-speed imaging studies and acoustic measurements, Mater. Today 49 (Oct. 2021) 10–22, https://doi.org/10.1016/J.MATTOD.2021.05.005.
[15] S. Haar, et al., Enhancing the liquid-phase exfoliation of graphene in organic solvents upon addition of n-octylbenzene, Sci. Rep. 5 (1) (Nov. 2015) 1–9, https://doi.org/10.1038/srep16684, 2015 51.
[16] U. Khan, H. Porwal, A. Óneill, K. Nawaz, P. May, J.N. Coleman, Solvent-exfoliated graphene at extremely high concentration, Langmuir 27 (15) (Aug. 2011) 9077–9082, https://doi.org/10.1021/LA201797H/SUPPL_FILE/LA201797H_SI_001.PDF.
[17] Z. Li, et al., Mechanisms of liquid-phase exfoliation for the production of graphene, ACS Nano 14 (9) (Sep. 2020) 10976–10985, https://doi.org/10.1021/ACSNANO.0C03916/SUPPL_FILE/NN0C03916_SI_001.PDF.
[18] K.L. Ng, et al., Direct evidence of the exfoliation efficiency and graphene dispersibility of green solvents toward sustainable graphene production, *ACS Sustain. Chem. Eng.*, Dec. (2022), https://doi.org/10.1021/ACSSUSCHEMENG.2C03594.
[19] A.V. Tyurnina, et al., Environment friendly dual-frequency ultrasonic exfoliation of few-layer graphene, *Carbon N. Y.*, Sep. (2021), https://doi.org/10.1016/J.CARBON.2021.09.036.
[20] J.A. Morton, et al., Effect of temperature and acoustic pressure during ultrasound liquid-phase processing of graphite in water, JOM (J. Occup. Med.) 73 (12) (Dec. 2021) 3745–3752, https://doi.org/10.1007/S11837-021-04910-9/TABLES/1.
[21] A. Kaur, et al., Temperature as a Key Parameter for Graphene Sono-Exfoliation in Water, Ultrason. Sonochem, 2022.
[22] M. Khavari, A. Priyadarshi, A. Hurrell, K. Pericleous, D. Eskin, I. Tzanakis, Characterization of shock waves in power ultrasound, J. Fluid Mech. 915 (2021), https://doi.org/10.1017/JFM.2021.186.
[23] G.S.B. Lebon, I. Tzanakis, K. Pericleous, D. Eskin, Experimental and numerical investigation of acoustic pressures in different liquids, Ultrason. Sonochem. 42 (2018) 411–421, https://doi.org/10.1016/j.ultsonch.2017.12.002.
[24] Y. Shin, et al., Enhanced liquid phase exfoliation of graphene in water using an insoluble bis-pyrene stabiliser, Faraday Discuss 227 (Apr. 2021) 46–60, https://doi.org/10.1039/C9FD00114J, 0.
[25] I. Tzanakis, G.S.B. Lebon, D.G. Eskin, K.A. Pericleous, Characterizing the cavitation development and acoustic spectrum in various liquids, Ultrason. Sonochem. 34 (Jan. 2017) 651–662, https://doi.org/10.1016/j.ultsonch.2016.06.034.
[26] J. Kim, et al., Direct exfoliation and dispersion of two-dimensional materials in pure water via temperature control, Nat. Commun. 6 (1) (Sep. 2015) 1–9, https://doi.org/10.1038/ncomms9294, 2015 61.
[27] D.B. Khismatullin, Resonance frequency of microbubbles: effect of viscosity, J. Acoust. Soc. Am. 116 (3) (2004) 1463–1473, Sep, https://doi.org/10.1121/1.1778835.
[28] L. Qin, et al., Ultrafast synchrotron X-ray imaging and multiphysics modelling of liquid phase fatigue exfoliation of graphite under ultrasound, Carbon N. Y. 186 (Jan. 2022) 227–237, https://doi.org/10.1016/J.CARBON.2021.10.014.
[29] I. Tzanakis, M. Hadfield, I. Henshaw, Observations of acoustically generated cavitation bubbles within typical fluids applied to a scroll expander lubrication system, Exp. Therm. Fluid Sci. 35 (8) (2011) 1544–1554, https://doi.org/10.1016/j.expthermflusci.2011.07.005.
[30] V. Ciaravino, H.G. Flynn, M.W. Miller, Pulsed enhancement of acoustic cavitation: a postulated model, Ultrasound Med. Biol. 7 (2) (1981) 159–166, https://doi.org/10.1016/0301-5629(81)90005-3.
[31] C. Delacour, C. Lutz, S. Kuhn, Pulsed ultrasound for temperature control and clogging prevention in micro-reactors, Ultrason. Sonochem. 55 (2019) 67–74, https://doi.org/10.1016/j.ultsonch.2019.03.012.
[32] M. Khavari, et al., Cavitation-Induced Shock Wave Behaviour in Different Liquids, Ultrason. Sonochem., 2022.
[33] S. Haar, et al., Enhancing the liquid-phase exfoliation of graphene in organic solvents upon addition of n-octylbenzene, Sci. Rep. 5 (1) (Nov. 2015) 1–9, https://doi.org/10.1038/srep16684, 2015 51.
[34] M. Dular, Hydrodynamic cavitation damage in water at elevated temperatures, Wear 346 (347) (Jan. 2016) 78–86, https://doi.org/10.1016/J.WEAR.2015.11.007.
[35] Y. Hernandez, M. Lotya, D. Rickard, S.D. Bergin, J.N. Coleman, Measurement of multicomponent solubility parameters for graphene facilitates solvent discovery, Langmuir 26 (5) (Mar. 2010) 3208–3213, https://doi.org/10.1021/LA903188A/SUPPL_FILE/LA903188A_SI_001.PDF.
[36] G.S.B. Lebon, I. Tzanakis, K. Pericleous, D. Eskin, P.S. Grant, Ultrasonic liquid metal processing: the essential role of cavitation bubbles in controlling acoustic streaming, Ultrason. Sonochem. 55 (Jul. 2019) 243–255, https://doi.org/10.1016/J.ULTSONCH.2019.01.021.
[37] I. Tzanakis, M. Hodnett, G.S.B. Lebon, N. Dezhkunov, D.G. Eskin, Calibration and performance assessment of an innovative high-temperature cavitometer, Sensor Actuator Phys. 240 (Apr. 2016) 57–69, https://doi.org/10.1016/J.SNA.2016.01.024.
[38] L. Yusuf, M.D. Symes, P. Prentice, Characterising the cavitation activity generated by an ultrasonic horn at varying tip-vibration amplitudes, Ultrason. Sonochem. 70 (Jan. 2021) 105273, https://doi.org/10.1016/J.ULTSONCH.2020.105273.
[39] R. Salinas, J. Pla-Franco, E. Lladosa, J.B. Montön, Density, speed of sound, viscosity, and excess properties of binary mixtures formed by ethanol and bis (trifluorosulfonyl)imide-based ionic liquids, J. Chem. Eng. Data 60 (3) (Mar. 2015) 525–540, https://doi.org/10.1021/JE500594Z/ASSET/IMAGES/JE500594Z.SOCIAL.JPEG_V03.
[40] I.S. Khattab, F. Bandarkar, M.A.A. Fakhree, A. Jouyban, Density, viscosity, and surface tension of water+ethanol mixtures from 293 to 323K, Kor. J. Chem. Eng. 29 (6) (Jan. 2012) 812–817, https://doi.org/10.1007/S11814-011-0239-6, 2011 296.
[41] V.A. Del Grosso, C.W. Mader, Speed of sound in pure water, J. Acoust. Soc. Am. 52 (5B) (Aug. 2005) 1442, https://doi.org/10.1121/1.1913258.
[42] M. Yusuf, M. Kumar, M.A. Khan, M. Sillanpääillanpa, H. Arafat, A review on exfoliation, characterization, environmental and energy applications of graphene and graphene-based composites, Adv. Colloid Interface Sci. 273 (Nov. 2019) 102036, https://doi.org/10.1016/J.CIS.2019.102036.
[43] C. Backes, et al., Spectroscopic metrics allow in situ measurement of mean size and thickness of liquid-exfoliated few-layer graphene nanosheets, Nanoscale 8 (7) (2016) 4311–4323, Feb, https://doi.org/10.1039/C5NR08047A.
[44] M. Ayán-Varela, J.I. Paredes, S. Villar-Rodil, R. Rozada, A. Martínez-Alonso, J.M. D. Tascón, A quantitative analysis of the dispersion behavior of reduced graphene oxide in solvents, Carbon N. Y. 75 (Aug. 2014) 390–400, https://doi.org/10.1016/J.CARBON.2014.04.018.
[45] L.M. Malard, M.A. Pimenta, G. Dresselhaus, M.S. Dresselhaus, Raman spectroscopy in graphene, Phys. Rep. 473 (5–6) (Apr. 2009) 51–87, https://doi.org/10.1016/J.PHYSREP.2009.02.003.
[46] X. Cong, X.L. Liu, M.L. Lin, P.H. Tan, Application of Raman spectroscopy to probe fundamental properties of two-dimensional materials, NPJ 2D Mater. Appl. 4 (1) (May 2020) 1–12, https://doi.org/10.1038/s41699-020-0140-4, 2020 41.
[47] A.C. Ferrari, D.M. Basko, Raman spectroscopy as a versatile tool for studying the properties of graphene, Nat. Nanotechnol. 8 (4) (Apr. 2013) 235–246, https://doi.org/10.1038/nnano.2013.46, 2013 84.
[48] A.C. Ferrari, et al., Raman spectrum of graphene and graphene layers, Phys. Rev. Lett. 97 (18) (Oct. 2006) 187401, https://doi.org/10.1103/PHYSREVLETT.97.187401/FIGURES/3/MEDIUM.
[49] A. Eckmann, et al., Probing the nature of defects in graphene by Raman spectroscopy, Nano Lett. 12 (8) (2012) 3925–3930, Aug, https://doi.org/10.1021/NL300901A/SUPPL_FILE/NL300901A_SI_001.PDF.
[50] S. Deng, V. Berry, Wrinkled, rippled and crumpled graphene: an overview of formation mechanism, electronic properties, and applications, Mater. Today 19 (4) (May 2016) 197–212, https://doi.org/10.1016/J.MATTOD.2015.10.002.
[51] C.B. Carter, D.B. Williams, Transmission electron microscopy: diffraction, imaging, and spectrometry, Transm. Electron Microsc. Diffraction, Imaging, Spectrom. (Aug. 2016) 1–518, https://doi.org/10.1007/978-3-319-26651-0/COVER.